Stationary residual layers in buoyant Newtonian displacement flows

S. M. Taghavi,[1] T. Séon,[2,a)] K. Wielage-Burchard,[2] D. M. Martinez,[1] and I. A. Frigaard[2,3]
[1]*Department of Chemical and Biological Engineering, University of British Columbia, 2360 East Mall, Vancouver, British Columbia V6T 1Z3, Canada*
[2]*Department of Mathematics, University of British Columbia, 1984 Mathematics Road, Vancouver, British Columbia V6T 1Z2, Canada*
[3]*Department of Mechanical Engineering, University of British Columbia, 6250 Applied Science Lane, Vancouver, British Columbia V6T 1Z4, Canada*

(Received 28 June 2010; accepted 17 March 2011; published online 26 April 2011)

We study buoyant displacement flows with two miscible fluids of equal viscosity in ducts that are inclined at angles close to horizontal ($\beta \approx 90°$). As the imposed velocity ($\hat{V}_0$) is increased from zero, we change from an exchange flow dominated regime to a regime in which the front velocity ($\hat{V}_f$) increases linearly with $\hat{V}_0$. During this transition, we observed an interesting phenomenon in which the layer of displaced fluid remained at the top of the pipe (diameter $\hat{D}$) during the entire duration of the experiment, apparently stationary for times $\hat{t} \gtrsim 10^3 \hat{D}/\hat{V}_0$ (the stationary residual layer). Our investigation revealed that this flow marks the transition between flows with a back flow, counter to the imposed flow, and those that displace instantaneously. The same phenomena are observed in pipes (experiments) and in plane channels (two-dimensional numerical computations). A lubrication/thin-film model of the flows also shows the transition from back flow to instantaneous displacement. At long times, this model has a stationary residual layer solution of the type observed, which is found at a unique ratio χ of the axial viscous velocity to the imposed velocity. The prediction of the stationary residual layer from the lubrication model is compared with the transition in observed behavior in our pipe flow experiments and our 2D numerical displacements in the channel. Reasonable agreement is found for the pipe and excellent agreement for the channel. Physically, in either geometry at transition, the upper layer of the fluid is in a countercurrent motion with zero net volumetric flux; the velocity at the interface is positive, but the velocity of the interface is zero. This results from a delicate balance between buoyancy forces against the mean flow and viscous forces in the direction of the mean flow. © *2011 American Institute of Physics*.
[doi:10.1063/1.3581063]

I. INTRODUCTION

We consider displacement flows in near-horizontal ducts (pipes and plane channels) with a heavier fluid displacing a lighter fluid downwards, i.e., density unstable. We have already presented preliminary results of our experimental work,[1] in which we studied the effects of augmenting a density unstable pipe exchange flow with an increasingly strong imposed mean flow. We were able to identify three distinct regimes: (i) an exchange flow dominated regime, (ii) a laminarised viscous displacement regime, and (iii) a fully mixed displacement regime. This paper presents an in-depth study into the physics of the transition between the first two of these regimes.

In the exchange flow context, the driving force is the buoyancy and the physical mechanisms that limit the flow are either inertia or viscosity, depending on the geometric configuration and the type of fluids.[2] Two characteristic velocities can be defined. First, a viscous velocity scale $\hat{V}_\nu$

$$\hat{V}_\nu = \frac{At\hat{g}\hat{D}^2}{\hat{\nu}} \tag{1}$$

when buoyancy and viscous term are balanced. Second, an inertial velocity scale $\hat{V}_t$

$$\hat{V}_t = \sqrt{At\hat{g}\hat{D}} \tag{2}$$

when buoyancy and inertia terms are balanced. Here, At is the Atwood number, defined as the ratio of the difference of densities of the two fluids by their sum, $\hat{g}$ is the acceleration due to gravity, $\hat{D}$ is the diameter of the pipe, and $\hat{\nu}$ is the common kinematic viscosity of the fluids, defined with the mean density.[3] Exchange flows have been classified as either *inertial* or *viscous* according to which effect is dominant in balancing buoyancy forces.[4] Inertial exchange flows are found in pipes if

$$\frac{\hat{V}_\nu \cos\beta}{\hat{V}_t} \gtrapprox 50, \tag{3}$$

and viscous exchange flows otherwise. Here, β measures the inclination of the pipe from vertical. Taghavi *et al.*[1] found that at sufficiently low mean imposed velocity $\hat{V}_0$, the flow

a)Author to whom correspondence should be addressed. Electronic mail: thomas.seon@gmail.com.

was close to an exchange flow, as expected. The measured downstream (or leading) front velocities ($\hat{V}_f$) were consistent with those of exchange flows in near-horizontal pipes.

At larger imposed $\hat{V}_0$, we find that the leading displacement front propagates at speed $\hat{V}_f$ that increases linearly with $\hat{V}_0$ (with slope larger than 1). This intermediate regime involves a laminarization of the flow, even when the underlying exchange flow configuration is inertial, indicating the dominance of viscous forces. A well defined interface is observed even for relatively high Reynolds numbers. In this viscous dominated regime, with the interface elongated along the duct, a natural modeling approach is the lubrication/thin-film approach, which we have developed for the simpler plane channel geometry.[5] Analysis of this model reveals that after a short transient, stable displacement flows of long aspect ratio are characterized by one or more steadily moving fronts that stretch the interface between them. For large buoyancy effects relative to the mean flow, one of the fronts propagates backward at the top of the channel against the mean flow. The frontal heights and speeds can be calculated straightforwardly for a wide range of different fluid rheologies and density differences.

Considering the transition between regimes (i) and (ii) (exchange flow and imposed flow dominated regimes), due to the density difference we always expect a stratified interface with heavier displacing fluid moving below the lighter fluid as it displaces. Denoting the flow rates of heavy and light fluids through a given cross-section by $\hat{Q}$ and $\hat{Q}_l$, respectively, we always have

$$\frac{\pi \hat{D}^2 \hat{V}_0}{4} = \hat{Q} + \hat{Q}_l. \tag{4}$$

At $\hat{V}_0=0$, we have $\hat{Q}_l=-\hat{Q}<0$ in the exchange flow. As $\hat{V}_0$ is increased, the net buoyancy force available to resist motion in the imposed flow direction remains constant, but the imposed flow creates viscous stresses that act on the lighter fluid layer at the interface and drag the lighter fluid along the duct. The viscous drag increases with $\hat{V}_0$ and eventually we expect to attain a transition where $\hat{Q}_l=0$, and thereafter $\hat{Q}_l>0$.

We believe the above to be an obvious feature of this transition. Less obvious is that the flow structures remain stationary at the transition; i.e., the layer thickness of the lighter fluid that is found at the transition is one for which the interface speed is zero. The flow apparently evolves to select this interfacial position so that the flow structures observed for $\hat{V}_0$ close to the transition persist over very long timescales (as described in detail in Sec. II B). This unexpected feature occurs in both experimental (pipe) and computational (plane channel) flows and is clearly of practical consequence, particularly for industrial displacements. Our paper fully explains this phenomenon and other aspects of the transition.

Although unexpected, we have found two parallels to this phenomenon in the literature. Huppert and Woods[6] considered a range of porous media flows driven by density difference, using a lubrication approximation. Part of their study considers two-layer exchange flows between reservoirs and among the solutions investigated there exist those for which the flow in one layer is zero. There are many differences between porous media flows and those governed by the Navier–Stokes equations. In the present context, we note that the main differences are that in porous media flows of Huppert and Woods,[6] zero flow in one fluid layer means the velocity is zero everywhere in that layer and the modified pressure gradient is also zero. In the Navier–Stokes context (our paper), there is a positive pressure gradient driving the light fluid layer backward against the flow and the velocities are nonzero within the stationary layer. In looking simply at lubrication-type models with an imposed flow, those based on underlying Hele–Shaw (or porous media) mechanics allow steady state interface propagation at the imposed velocity,[7] whereas those based on the Navier–Stokes systems do not.[5]

The second parallel concerning stationary layers comes from consideration of non-Newtonian fluid rheologies and, in particular, fluids with a yield stress. In displacement flows of such fluids, it is relatively common for there to remain behind stationary layers attached to the wall.[8] This occurs also in the context of buoyancy dominated displacements.[5] As with the porous media displacements, unyielded stationary layers also have zero velocity everywhere. However, in contrast to porous media displacements (also to the Navier–Stokes displacements we consider here), stationary layers are found over a finite range of thicknesses and net pressure gradients, whenever the fluid yield stress is strong enough to resist motion.

A more general motivation for our paper arises since buoyancy driven flows of miscible Newtonian fluids over near-horizontal surfaces occur frequently in the oceanographic, meteorological, and geophysical contexts,[9,10] i.e., gravity currents. Most frequently, these flows have been studied in unconfined geometries.[11–15] More recently, due to the importance of these flows in the industrial world, confined geometries such as a vertical[16–19] or inclined pipe[2,4,20–22] have been considered.

On entering the industrial arena, it is natural to consider the imposition of a mean flow. Indeed, in this context one can regard the displacement of one fluid with another as the archetypical flow, which is modified by density differences between the fluids. The study of miscible laminar displacement flows in ducts is less mature than that of gravity currents. Although dispersive regimes were first studied over 50 years ago,[23,24] many practical processing situations involving aqueous liquids in laminar duct flows are far from this regime. In an industrial setting, probably the most relevant laminar regime is the nondispersive high Péclet number regime, where the ducts have long aspect ratios but still lie well below the Taylor dispersion regime. This high Péclet number regime has been studied analytically, computationally, and experimentally[25–28] in the case of isodense fluids. These studies show that sharp interfaces persist over wide ranges of parameters for dimensionless times (hence lengths) smaller than the Péclet number. At longer times (lengths) the dispersive limit is attained. For fixed lengths and increasing

Péclet number (while remaining laminar), the flow is comparable to an immiscible displacement (with zero-surface tension).

Industrial displacement flows often involve both density differences between fluids and rheological differences (which we do not consider here). With buoyancy, there are a number of displacement studies in vertical ducts, both for miscible and immiscible fluids,[29–32] but here we focus exclusively on near-horizontal inclinations, which are phenomenologically different in that near-stratified viscous regimes are more prevalent. Many different types of industrial displacement flow arise. Turbulent displacing regimes are typically more effective, but are not always possible due to process constraints; here our flows are laminar. A second distinction comes in the volume of displacing fluid that is used. In some processes, an essentially continuous stream can be pumped through the duct, e.g., water in turbomachinery, and there are few time restrictions. In other processes, due to either disposal issues or cost of the fluids, it is desirable to displace the *in situ* fluid with more or less a single "duct volume" of fluid; i.e., we are replacing the *in situ* fluid with another.

An example of the latter process is the primary cementing of oil and gas wells,[33] which motivated our study. This process involves displacing one fluid with another or with a sequence of different fluids. The geometries are typically pipe, annular, or duct-like, all with long aspect ratios. Large volumes are pumped so that fluids may be considered separated; i.e., we have a two-fluid displacement, not an *n*-fluid displacement. A very wide range of fluids are used. Significant density differences can occur; shear-thinning and yield stress rheological behaviors are widely found. The main aim of the process is to fully replace the *in situ* drilling mud with a cement slurry. Our study highlights a particular displacement regime where this type of process objective may fail.

An outline of the paper follows. Section II presents the results of our study in the pipe geometry. The experimental setup is explained and observations presented, focusing particularly on the back flow region. This is followed by development of a lubrication/thin-film model for the pipe geometry. This model is used to make quantitative predictions that are in reasonable agreement with our experimental data. In the second part of the paper (Sec. III), we study the same phenomenon, but in the simpler plane channel geometry. Here, the lubrication model leads directly to analytic predictions of the stationary layer. These predictions are compared with results from fully two-dimensional (2D) computations of the displacement flows in this regime. An excellent agreement is found. The paper concludes with a discussion. In the appendix, we outline a simple physical model based only on a momentum balance that is able to give the same qualitative behaviors.

II. PIPE DISPLACEMENTS

A. Experimental setup and procedure

The study was performed in a 4 m long 19.05 mm diameter transparent pipe with a gate valve located 80 cm from one end [Fig. 1(a)]. The pipe was mounted on a frame that could be tilted at any chosen angle. Initially, the lower part of

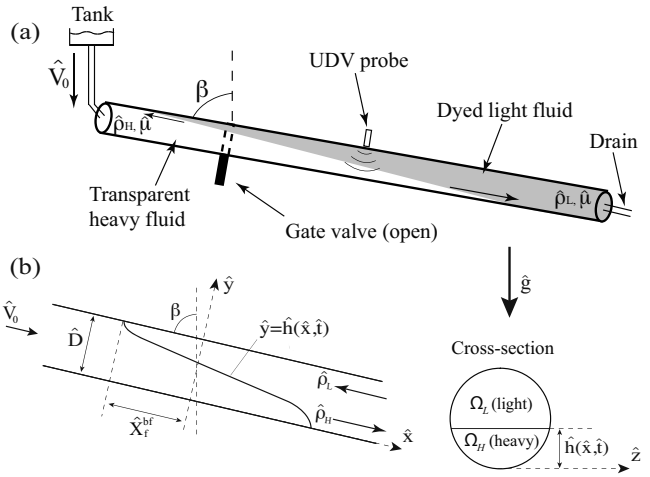

FIG. 1. (a) Schematic view of the experimental setup. The shape of the interface is illustrative only. More realistic shapes are given in Fig. 3 where the interface shape was found to evolve both spatially and temporally. The arrows in the diagram represent the motion of the fronts. (b) Schematic views of the distribution of the two fluids in two perpendicular vertical planes of the pipe (diametrical and transversal). The notation is that used later in our models.

the pipe was filled with water colored with a small amount of ink and the upper part by a denser salt-water solution. The pipe was fed by gravity from an elevated tank. The imposed flowrate was controlled by a valve and measured by both a rotameter and a magnetic flowmeter located downstream of the pipe. Experiments were performed using water as the common fluid, with salt (NaCl) added to one of the fluids in order to increase its density. A large number of experiments were conducted over the ranges of $[\hat{V}_0,\ At,\ \beta] \in [0-80\ \text{mm}\cdot\text{s}^{-1},\ 10^{-3}-10^{-2},\ 83°-87°]$. Our imaging system consisted of two digital cameras with images recorded at a frame rate of 2–4 Hz. The pipe was back-lit, and after opening the valve, images were obtained at regular time intervals, which enabled us to create spatiotemporal diagrams of the concentration profiles along the length of the pipe. The displacement of the front was marked on these diagrams by a sharp boundary between the gray shades corresponding to the two fluids. The front velocity was obtained from the slope of this boundary.

We also measured the velocity profile at 80 cm below the gate valve, using an ultrasonic Doppler velocimeter DOP2000 (model 2125, Signal Processing SA) with 8 MHz 0.5 cm (TR0805LS) transducers. It is based on the pulse-echo technique and allows the measurement of the flow velocity projection on the ultrasound beam in real time.[34] We used polyamid seeding particles with a mean particle diameter of 50 μm. The probe was mounted at an angle 78° relative to the axis of the pipe.

B. Experimental observations

Before giving a broad description of our general results, we describe in detail the experimental observation that motivated our deeper investigation. In systematically increasing the mean flow velocity $\hat{V}_0$ from zero, we came across flows in which the downstream layer of *in situ* fluid remained ap-

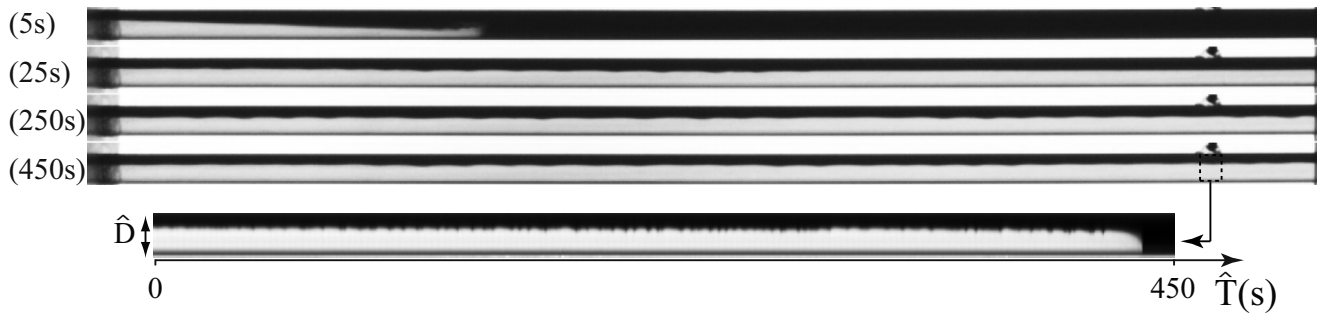

FIG. 2. Sequence of images showing the stationary upper layer. This sequence is obtained for 5, 25, 250, and 450 s after opening the gate valve. The field of view is 1015×20 mm and taken right below the gate valve. For this experiment, the pipe is tilted at 85° from vertical. The normalized density contract is $At=10^{-2}$, the viscosity is $\hat{\mu}=10^{-3}$ Pa·s, and the mean flow velocity is $\hat{V}_0=38$ mm·s^{-1}. The figure below the sequence is a spatiotemporal diagram of the variation of the light intensity in the transverse dimension, averaged over 20 pixels along the pipe in the region marked on the pipe above, with a time step of $\Delta\hat{t}=0.5$ s. It shows the variation of the layer height with time.

parently stationary and uniform at the top of the pipe, while the displacing fluid traveled underneath.

Figure 2 displays an example of such a flow in the configuration where a heavy fluid (transparent) is injected to displace the lighter fluid (black), which is initially filling the inclined pipe. The displacement is from left to right. The leading front of the heavy fluid slumps underneath the light fluid at the start of the displacement (first image). We observe that 25 s after the beginning of the process, the two fluids are stratified along the length of the pipe. Since only the transparent fluid is injected, it is obvious that the two layers have different mean velocities and intuitively we would not expect this configuration to remain stationary. However, looking at the next two images (250 and 450 s) we observe that the upper layer retains the same thickness. The image at the bottom of Fig. 2 is a spatiotemporal diagram of the light intensity across the pipe (averaged over the small square marked on the fourth image). The horizontal scale is time and the vertical scale is the pipe diameter. At $\hat{t}=0$, the image is all black because the pipe is full of black fluid. After around 15 s, the heavy fluid arrives in this part of the pipe and we observe on the spatiotemporal diagram the two layers with the transparent fluid below the black fluid. The thickness of the layers stays constant until the end of the experiment, about 7 min.

The surprising feature of this observation was the longevity of the upper layer, outliving the duration of our experiment. During the time of the experiment in Fig. 2, five times the volume of the pipe have flowed through the pipe. Alternatively, the layers are constant for $\sim10^3$ times the advective timescale $\hat{D}/\hat{V}_0\approx0.5$ s. Also unexpected, but found only after our analysis, was that the interfacial velocity (i.e., wave speed of the interface) is zero so that the stationary layer is not simply a consequence of the flow becoming near-parallel.

We turn now to a more general description of our results. On closer investigation it became evident that as $\hat{V}_0$ was increased from zero, the most obvious changes in the flow occurred above the gate valve with the *trailing* front, rather than below with the leading front (which typically was quickly advected out of the 4 m pipe). The trailing or upstream front (meaning upstream of the mean flow) exhibited four different characteristic behaviors. Figure 3 illustrates these four behaviors in a 1015 mm long section of the pipe, tilted at $\beta=85°$, for a sequence of displacements at the same density difference ($At=10^{-2}$) but at different $\hat{V}_0$. In each image, the heavier transparent fluid moves downward from left to right; the black part at the right of each image is the gate valve and in the middle is a bracket supporting the pipe.

In Fig. 3(a), the lighter fluid is moving upward against the imposed flow and the front moves steadily upstream without stopping. This picture was taken a few seconds after the tip of the front reached the upper end of the experimental

FIG. 3. Four snapshots of video images taken at different mean flow rates and illustrating the different regimes. The heavy transparent fluid flows downward under the combined effects of buoyancy ($\Delta\rho$) and pressure gradient ($\hat{V}_0$). The light black fluid has different behaviors (flows upward or downward) depending on the control parameters values. These images were obtained at $\beta=85°$, $At=10^{-2}$, and $\hat{\mu}=10^{-3}$ Pa·s. The mean flow velocities were: (a) $\hat{V}_0=29$ mm·s^{-1}, (b) $\hat{V}_0=38$ mm·s^{-1}, (c) $\hat{V}_0=42$ mm·s^{-1}, and (d) $\hat{V}_0=61$ mm·s^{-1}. The field of view is 1015×20 mm, and contains the gate valve (wide black stripe) and a pipe support (thin black stripe). The images are taken at: (a) 150 s, (b) 290 s, (c) 365 s, and (d) 75 s after opening the valve.

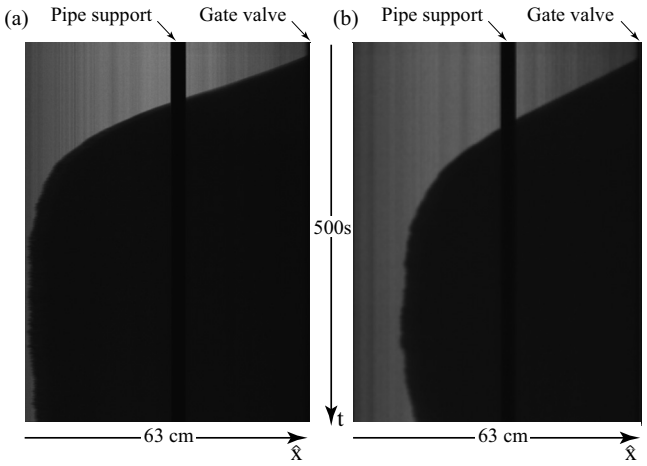

FIG. 4. Spatiotemporal diagrams of the variation of the light intensity along a line parallel to the pipe axis in the upper section of the pipe. The vertical scale is time ($\Delta\hat{t}$=0.5 s and 500 s for both) and the horizontal scale is the distance along the pipe above the gate valve (see Fig. 3). The orientation of the x axis is the same as in Fig. 3: downward. These diagrams correspond to the experiments: (a) Fig. 3(b) ($\hat{V}_0$=38 mm·s^{-1}) and (b) Fig. 3(c) ($\hat{V}_0$=42 mm·s^{-1}).

pipe. The low mean velocity ($\hat{V}_0$=29 mm·s^{-1}) allows a countercurrent flow similar to the exchange flow, except that the back flow moves slower. We describe such flows as sustained back flows; i.e., there is a sustained upstream flow that advects the trailing front continually upstream against the mean flow.

In Fig. 3(b), with an increased imposed flow ($\hat{V}_0$ =38 mm·s^{-1}) we observe that the trailing front moves initially upstream against the flow, but then stops moving. This picture was taken 60 s after the front stopped when it was stationary (290 s after the beginning of the experiment). This is the same experiment as in Fig. 2, for which the thickness of the upper layer in the downstream part of the pipe remains constant for a long time. We classify such flows as stationary interface flows.

In the next image [Fig. 3(c)], with a slightly higher mean velocity ($\hat{V}_0$=42 mm·s^{-1}) the trailing front moves upstream and stops, but closer to the initial position. The front stays in this position for a while but is eventually displaced downstream. We classify this behavior as a temporary back flow; i.e., there is a flow backward against the mean flow that initially advects the trailing front upstream but the back flow is not sustained over long times. Finally, if the mean velocity is further increased [Fig. 3(d)], the trailing front between clear and dark fluid is simply displaced downstream. We call this high mean flow case an instantaneous displacement, ($\hat{V}_0$=61 mm·s^{-1}).

For a more in-depth look at the transition between the stationary interface and the instantaneous displacement regimes, we display spatiotemporal diagrams of the back flows corresponding to Figs. 3(b) and 3(c) in Figs. 4(a) and 4(b), respectively. These spatiotemporal diagrams are realized along a line in the upper part of the pipe section, where the back flow rises. The vertical scale depicts time (500 s in each figure) and the horizontal scale denotes distance along the pipe, from just above the gate valve. The instantaneous front velocities are determined from the local slope of the boundaries separating the black regions of the diagram (back flow zones) from the gray regions (transparent fluid). We observe in Fig. 4(a) that the back flow starts with a constant velocity and then slows down until it stops. It does not move significantly until the end of the experiment (except for small longitudinal oscillations). As the interface of the upper layer is stationary, this demonstrates that throughout this period we have a balance between the pressure driven flow and the buoyant flow. For a slightly increased imposed flow we observe in Fig. 4(b) the temporary back flow regime. The back flow stops closer to the gate valve and starts to be displaced downward before the end of the experiment. Longer times are not shown on this figure but the back flow is displaced until its original position (the gate valve) and beyond. These behaviors will be interpreted in the next section. A closer inspection of Fig. 4(a) at long times shows a small deviation of the boundary from vertical, smaller but in the same direction as Fig. 4(b). This may indicate the slow onset of temporary back flow.

Figure 5 displays transverse profiles of the longitudinal velocity (parallel to the pipe axis) averaged over time for three regimes: sustained back flow [Fig. 5(a)], stationary interface [Fig. 5(b)], and instantaneous displacement [Fig. 5(c)]. These are measured below the gate valve along a line passing through the center of the pipe. The vertical scale represents the distance from the upper wall and the horizontal scale is the longitudinal velocity component, with positive values measured in the flow direction. The horizontal dashed line shows the position of the interface. Close to the lower wall there are instrumental errors: an oblique dashed line has been added to artificially complete the profile to the wall, where the velocity is zero.

First of all, we observe that the three figures show a downward global net flow due to the mean flow. By looking specifically at each regime, we observe that in the back flow regime [Fig. 5(a) corresponding to the experiment of Fig. 3(a)] the velocity at the interface is small. Almost the entire upper layer moves upstream. In the stationary interface regime [Fig. 5(b) corresponding to the experiment of Fig. 3(b)], we observe that the fluid velocity at the interface is positive, but that both positive and negative velocities are found in the upper layer. Therefore, although the interface is apparently stationary, the fluid in the upper layer is not motionless but moves in a countercurrent recirculatory motion. The displacing fluid is observed to pass underneath the upper layer and so we expect that the net flow rate through the upper layer should be very close to zero. This measurement is averaged along a transverse axis positioned centrally in the pipe cross-section. Although plausibly close to zero, the measurements are not precise enough to evaluate this zero net flow condition. Additionally, there are variations in the z-direction that would need estimating or measuring. Finally, in the instantaneous displacement regime [Fig. 5(c)] the lighter fluid has been mostly displaced, leaving only a very thin residual layer.

The above constitutes a description of the distinct flow

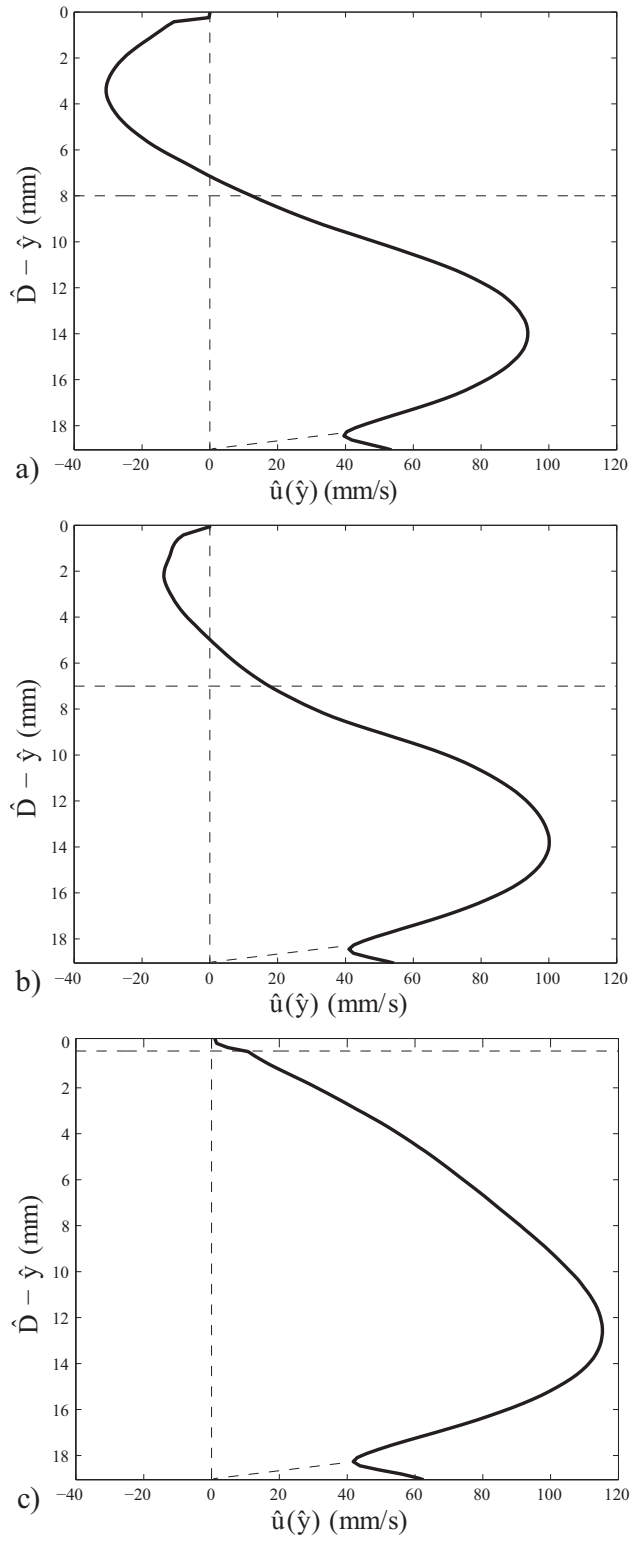

FIG. 5. Ultrasonic Doppler velocimeters profiles for the same series of experiments as Fig. 3: (a) $\hat{V}_0=29$ mm·s^{-1} [see Fig. 3(a)] sustained back flow regime, profiles averaged between 60 and 120 s; (b) $\hat{V}_0=38$ mm·s^{-1} [see Fig. 3(b)] stationary interface regime, profiles averaged between 240 and 300 s; and (c) $\hat{V}_0=74$ mm·s^{-1} instantaneous displacement regime, profiles averaged between 120 and 240 s. The vertical scale represents the distance from the upper wall ($\hat{y}$ measuring distance from the lower one) and the horizontal scale the corresponding value of the longitudinal flow velocity. The horizontal dashed line shows the position of the interface. The vertical dashed line shows the zero velocity. The oblique dashed line close to the lower wall has been added to guide the eye where the profiles are distorted by instrumental error.

regimes observed in our experiments, as $\hat{V}_0$ is varied. One could say that we have essentially three regimes, with the stationary layer apparently representing a transition state between flows with sustained back flow and those that displace. Below in Sec. II C, we derive a simple model that predicts similar flow regimes and transitions. In Sec. II D, we present the comparison between the predictions of this model and the classification of our experiments.

C. Lubrication model

Our experimental observations suggest that (after the initial few seconds of our displacements and away from the tips of the leading/trailing fronts) most of the flow occurs within regions where the fluids are separated by interfaces that are aligned approximately with the pipe axis. It is therefore very natural to develop a thin-film/lubrication style model for the pipe displacement flow. The procedure is more or less standard and we follow largely that of our previous work.[5] At each axial position $\hat{x}$, the flow is assumed stratified with the interface denoted as $\hat{y}=\hat{h}(\hat{x},\hat{t})$; see the geometry illustrated schematically in Fig. 1(b). The leading order equations are the momentum balances

$$0=-\frac{\partial\hat{p}}{\partial\hat{z}}, \tag{5}$$

$$0=-\frac{\partial\hat{p}}{\partial\hat{y}}-\hat{\rho}_k\hat{g}\sin\hat{\beta}, \tag{6}$$

$$0=-\frac{\partial\hat{p}}{\partial\hat{x}}+\hat{\mu}\left[\frac{\partial^2\hat{w}}{\partial\hat{z}^2}+\frac{\partial^2\hat{w}}{\partial\hat{y}^2}\right]+\hat{\rho}_k\hat{g}\cos\hat{\beta},$$
$$(\hat{z},\hat{y})\in\Omega_k k=H,L \tag{7}$$

and the incompressibility condition, $\nabla\cdot\hat{\mathbf{u}}=0$. At the walls, $\hat{\mathbf{u}}=0$ and both velocity and traction vectors are continuous at the interface. For the flows considered, a mean flow $\hat{V}_0$ is imposed by pumping in the positive $\hat{x}$-direction. Thus, the additional constraint

$$\frac{\pi\hat{D}^2\hat{V}_0}{4}=\int_{\Omega_H\cup\Omega_L}w d\hat{z}d\hat{y}, \tag{8}$$

is satisfied by the solution. We eliminate $\hat{p}$ and derive the evolution equation for $\hat{h}$

$$\frac{\partial}{\partial\hat{t}}\hat{A}(\hat{h})+\frac{\partial}{\partial\hat{x}}\hat{Q}=0, \tag{9}$$

where $\hat{A}(\hat{h})$ is the area occupied by the heavier fluid, $\hat{A}(\hat{h})=|\Omega_H|$, and

$$\hat{Q}=\int_{\Omega_H}\hat{w}d\hat{z}d\hat{y}. \tag{10}$$

The flux consists of a superposition of Poiseuille and exchange flow components

$$\hat{Q} = \hat{Q}(\hat{h}, \hat{h}_{\hat{x}})$$
$$= 2\hat{V}_0 \int_{\hat{A}(\hat{h})} \left(1 - 4\frac{\hat{z}^2 + \hat{y}^2}{\hat{D}^2}\right) d\hat{z}d\hat{y}$$
$$+ \frac{\pi\hat{D}^2}{8} F_0 \hat{V}_\nu \left(1 - 4\frac{(\hat{D}/2 - \hat{h})^2}{\hat{D}^2}\right)^{7/2} \left(\cos\beta - \sin\beta \frac{\partial\hat{h}}{\partial\hat{x}}\right),$$

where $\hat{V}_\nu = At \cdot \hat{g} \cdot \hat{D}^2/\hat{\nu}$ and F_0 is given[2] as $F_0 = 0.0118$. The exchange flow component has been estimated[2] by extrapolating from the value at $\hat{h} = \hat{D}/2$ and from asymptotic expressions for $\hat{h} \sim 0$ and $\hat{h} \sim \hat{D}$.

Taghavi *et al.*[5] defined dimensionless parameters δ and χ via

$$\delta = \frac{\hat{\mu}\hat{V}_0}{[\hat{\rho}_H - \hat{\rho}_L]\hat{g}\sin\hat{\beta}\hat{D}^2} = \frac{\hat{V}_0}{2\hat{V}_\nu \sin\beta},$$
$$\chi = \frac{\cot\beta}{\delta} = \frac{2\hat{V}_\nu \cos\beta}{\hat{V}_0}, \tag{11}$$

and scaled the system using a length-scale $\hat{L} = \hat{D}/\delta$ in the $\hat{x}$-direction, with $\hat{L}/\hat{V}_0$ as timescale. Here we adopt the same scalings and also scale $\hat{A}(\hat{h})$ with $\pi\hat{D}^2/4$, $\hat{Q}$ with $\pi\hat{D}^2\hat{V}_0/4$, and $(\hat{h}, \hat{y}, \hat{z})$ with $\hat{D}$. The resulting dimensionless equations are

$$\frac{\partial}{\partial T}\alpha(h) + \frac{\partial}{\partial\xi} q(h, h_\xi) = 0, \tag{12}$$

where $h \in [0,1]$ is now dimensionless, $\alpha(h) = 4\hat{A}(\hat{h})/\pi\hat{D}^2$ is the area fraction occupied by the heavy fluid

$$\alpha(h) = \frac{1}{\pi}\cos^{-1}(1-2h) - \frac{2}{\pi}(1-2h)\sqrt{h-h^2},$$
$$q(h, h_\xi) = \frac{32}{\pi}\int_{\alpha(h)} \left(\frac{1}{4} - x^2 - y^2\right) dxdy$$
$$+ \frac{F_0[\chi - h_\xi]}{4}[1 - (1-2h)^2]^{7/2},$$

T and ξ are the dimensionless time and length variables, respectively. This is the equivalent dimensionless equation to (2.23) in Ref. 5.

Although the algebraic form of Eq. (12) differs from that analyzed for the plane channel, we expect a similar behavior. Let us first consider the downstream behavior. At long times the interface is expected to elongate,[5] which negates the effect of the slope of the interface in all regions except local to the advancing frontal region. The behavior is approximated by the hyperbolic part of Eq. (12), i.e., setting $q = q(h,0)$. We have observed (Fig. 3) that the interface remains stationary for the duration of the experiment, with constant flow rate of displacing heavy fluid. In the context of Eq. (12), considered at long times, this implies that the interfacial speed is zero and the flux, $q(h,0) = 1$. The interfacial speed V_i is simply the characteristic speed

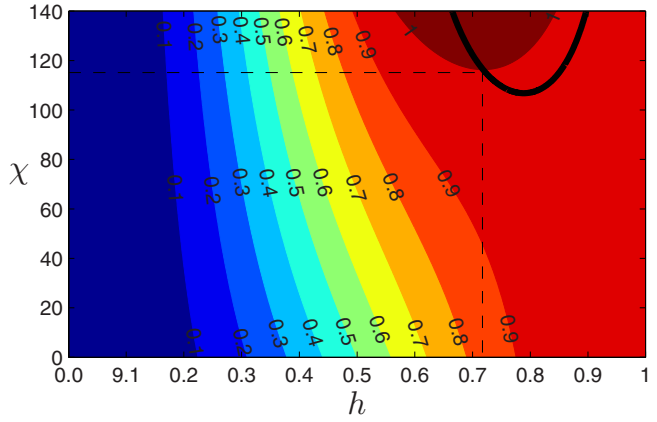

FIG. 6. (Color online) Contours of $q(h,0)$ and the contour $\partial q/\partial h(h,0) = 0$ (bold black line). The intercept of $q(h,0) = 1$ and $\partial q/\partial h(h,0) = 0$ occurs at $\chi = 116.32...$ and $h = 0.72...$.

$$V_i = \frac{\partial q}{\partial\alpha}(h,0) = \frac{\partial q}{\partial h}(h,0)\left[\frac{d\alpha}{dh}(h)\right]^{-1},$$

and since α is monotone with respect to h, the condition $V_i = 0$ implies that $\partial q/\partial h(h,0) = 0$. Note that $q(h,0)$ depends on the single parameter χ. In Fig. 6, we plot contours of $q(h,0)$ and the contour $\partial q/\partial h(h,0) = 0$, against (h,χ). The intercept of $q(h,0) = 1$ and $\partial q/\partial h(h,0) = 0$ occurs at a critical $\chi = \chi_c = 116.32...$ and for $h = 0.72...$, indicating that there is a unique interface height and value of χ for which stationary interfaces may occur.

Considering now the trailing front, for the plane channel displacement[5] large values of χ resulted in a second front propagating upstream against the flow, i.e., a back flow. Large χ corresponds to a weak imposed flow relative to the buoyancy driven exchange flow component. For the pipe flow, assuming again that the long time behavior is dominated by the hyperbolic part of Eq. (12), the equations determining the back flow front speed $V_f < 0$ and front height h_f, are simply

$$[1 - \alpha(h_f)]V_f = [1 - q(h_f, 0)], \tag{13}$$
$$V_f = \frac{\partial q}{\partial h}(h_f, 0)\left[\frac{d\alpha}{dh}(h_f)\right]^{-1}. \tag{14}$$

For sufficiently large χ this expression has solutions $V_f < 0$. We now observe that if we take the limit $V_f \to 0$ we also enforce $q(h_f, 0) = 1$. It follows that the conditions for the stationary interface are identical with those determining whether or not Eq. (12) has a sustained back flow: for $\chi > \chi_c$ we have sustained back flow and for $\chi < \chi_c$ there is no sustained back flow. Strictly speaking, both statements relate to longtime behavior of Eq. (12).

In Fig. 7, we plot $h(\xi, T)$ for the critical $\chi = \chi_c$, obtained by solving Eq. (12) numerically using the same method as in our previous work for the plane channel.[5] The trailing front at the top of the pipe is stationary as expected, while the leading front moves down the pipe. Although over long times the interface is stretched out between the stationary

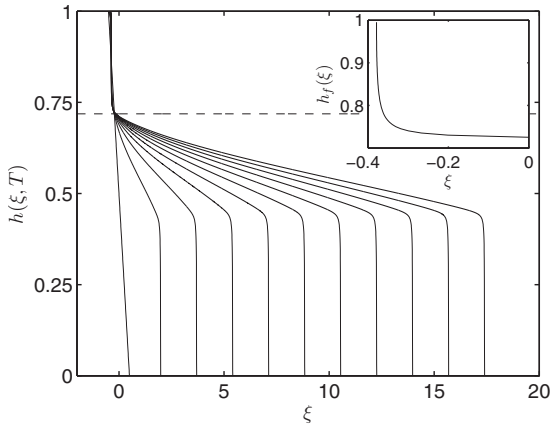

FIG. 7. Profiles of $h(\xi,T)$ for $T=0,1,\ldots,9,10$, with $\chi=\chi_c$. The broken line shows the theoretical stationary $h=0.72...$ at $\chi=\chi_c$. The inset shows the extension of the stationary frontal region.

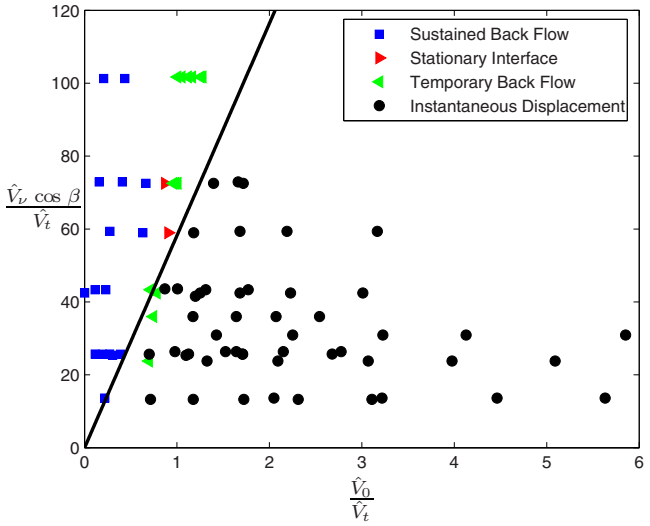

FIG. 8. (Color online) The experimental results in a pipe over the entire range of control parameters ($\hat{V}_0$ is in the range of $0-80$ mm$\cdot$s^{-1}, At is in the range of $10^{-3}-10^{-2}$, and β is in the range of 83°–87°). The heavy line represents the prediction of the lubrication model for the stationary interface: $58.16\,\hat{V}_0=\hat{V}_\nu\cos\beta$.

trailing front and the advancing leading front, the fronts are not shocks. By solving for each $h\in(h_f,1)$ the nonlinear equation

$$q(h,h_\xi)=0,$$

we may find the steady interface slope, $h_\xi(h)$. This can be integrated to find the shape of the steady profile for $h>h_f$. In this frontal region, buoyancy driven by the slope of the interface (acting to smooth the interface) is in balance with the buoyancy force driving fluid back up the inclined pipe. The frontal profile is illustrated in the inset of Fig. 7. The numerical integration has been stopped when h is within 1% of h_f.

D. Experimental and theoretical comparison

The analysis of the previous section suggests that stationary interfaces can occur for each inclination angle β only at a critical balance

$$\hat{V}_\nu\cos\beta\approx 58.16\hat{V}_0 \tag{15}$$

(recall $\chi=2\hat{V}_\nu\cos\beta/\hat{V}_0$). In the lubrication model context, sustained back flows are only found upstream for smaller values of $\hat{V}_0$ than in Eq. (15), whereas downstream the interface speed becomes positive for larger $\hat{V}_0$ than in Eq. (15) and instantaneous displacement ensues. Temporary back flows are not strictly covered by the long time analysis of the lubrication model.

Our experiments have been performed over the ranges

$$\hat{V}_0\in 0-80\ \text{mm}\cdot\text{s}^{-1},\quad At\in[10^{-3}-10^{-2}],$$

$$\beta\in[83^\circ-87^\circ].$$

To give an overall perspective of the different flow regimes and where they occur, Fig. 8 presents the classification of our flows for the full range of experiments. We observe that the sustained back flow regime is clearly separated from the instantaneous displacement regime. Between these two regimes we find stationary layers and temporary back flows. We must acknowledge potential errors in making the classifications depicted in Fig. 8. For example, sustained back flow experiments are terminated when the back flow exits the upper end of the pipe (due to ensuing mixing) but in a longer pipe could reverse and become temporary. Equally, the stationary interface case is clearly a marginal transition between sustained and temporary back flows. With a finite duration experiment (with other restrictions and errors), it is difficult to definitively classify a displacement as stationary. The bold line illustrates the analytical prediction Eq. (15). Given the potential uncertainty in classifying experiments and in the approximation of the exchange flow component of q, the prediction offered by this linear relation Eq. (15) is surprisingly good. We also note that in those experiments that we have classified as stationary interface flows, the stationary layer occupies ~30% of the pipe at the top, which corresponds well with the theoretical stationary $h=0.72...$ at $\chi=\chi_c$.

It is worth commenting that we have plotted our results in dimensionless velocity coordinates, with both $\hat{V}_0$ and $\hat{V}_\nu\cos\beta$ scaled with the inertial scale $\hat{V}_t$. This of course does not affect the relation between $\hat{V}_0$ and $\hat{V}_\nu\cos\beta$ that is exemplified in Fig. 8, but may appear strange for phenomena that are essentially viscous. This choice can be understood better in the context of previous work. The vertical axis shows the competition between viscous and inertial forces in balancing buoyancy, in the absence of any imposed flow. As discussed in Sec. I, pure exchange flow studies[4] have suggested that for $\hat{V}_\nu\cos\beta\gtrapprox 50\hat{V}_t$, the exchange flow is governed by an inertia-buoyancy balance (and viscous-buoyancy below this value). Our experiments cover this range and clearly the *viscous* prediction from Eq. (15) is still apparently relevant in what might be thought of as the inertial regime. The explanation for this comes from our previous work,[1] in which we have shown that the imposition of a mean flow results in the streamlines becoming progressively aligned with the pipe axis, even in this inertial regime. The consequent stabiliza-

tion as the flow rate (Reynolds number) is increased is somewhat counterintuitive. We can view Eq. (15) as being derived from the instantaneous displacement configuration in the regime $\hat{V}_\nu \cos\beta \gtrapprox 50\hat{V}_t$, and provided that $\hat{V}_0$ is large enough, the flows are sufficiently laminar and noninertial for the validity of the model.

III. PLANE CHANNEL GEOMETRY (2D)

In the preceding section, we have considered the pipe geometry, which is well suited to the experiment. Our attempts to quantify the stationary layer phenomenon via Eq. (15) are reasonable given experimental errors and the degree of approximation necessary for semianalytical theories. To confirm our explanation more fully, we could turn to computational simulation, but in the pipe geometry this investigation would require fully three-dimensional (3D) computations, which are exceedingly expensive computationally in pipes of long aspect ratio. Instead, therefore, we turn to a 2D plane channel geometry in order to confirm our understanding of the stationary layer. This geometry allows for faster computations and more precise asymptotic approximations. The channel has height $\hat{D}$ and is oriented similarly to the pipe, close to horizontal. Again, a heavy fluid displaces a lighter fluid in the downwards direction.

A. Lubrication model

The lubrication/thin-film approach is analogous to that developed for the pipe, leading to a dimensionless evolution equation for the interface height, $y=h(\xi,T)$

$$\frac{\partial h}{\partial T}+\frac{\partial}{\partial \xi}q(h,h_\xi)=0. \tag{16}$$

This has been derived and extensively studied by Taghavi *et al.*[5] for a wide range of fluid types. We focus only on the analysis relevant to the current situation. In parallel with the earlier analysis of Eq. (12), we may compute a critical value of χ and h for which the entire flux passes through the lower layer and for which the interface speed is zero. Contours of $q(h,0)$ and the contour $\partial q/\partial h(h,0)=0$ are plotted in (h,χ)-space in Fig. 9, from which we find $\chi_c=69.94$ for the plane channel at an interface height $h=0.707$. Note here that $h\in[0,1]$ as we have scaled with the height $\hat{D}$ of the channel. The relation $\chi=\chi_c$ again provides a predictor of the stationary interface, which we now test against 2D computational solutions.

B. Numerical method and overview

We have carried out a number of numerical simulations of 2D displacements in an inclined plane channel. The geometry and notation are as represented in Fig. 1(b) (neglecting the cross-sectional plane). Our computations are fully inertial, solving the full 2D Navier–Stokes equations. The phase change is modeled via a scalar concentration, c, which is advected with the flow; i.e., molecular diffusion is neglected. This neglect is due to the large Péclet numbers that correspond to our experimental flows, for which we typically have a well defined interface. The Navier–Stokes equations

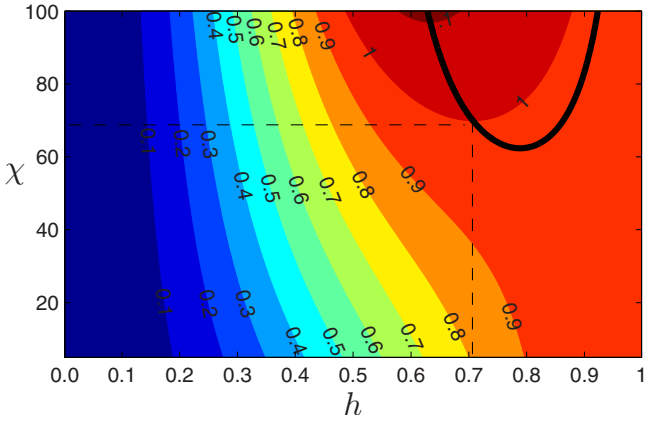

FIG. 9. (Color online) Contours of $q(h,0)$ and the contour $\partial q/\partial h(h,0)=0$ (bold black line), in a plane channel displacement. The intercept of $q(h,0)=1$ and $\partial q/\partial h(h,0)=0$ occurs at $\chi=\chi_c=69.94$ and $h=0.707$.

are made dimensionless using the channel height $\hat{D}$ as lengthscale and $\hat{V}_0$ as velocity scale. The model equations are

$$[1+\phi At][\mathbf{u}_t+\mathbf{u}\cdot\nabla\mathbf{u}]=-\nabla p+\frac{1}{Re}\nabla^2\mathbf{u}+\frac{\phi}{Fr^2}\mathbf{e}_g, \tag{17}$$

$$\nabla\cdot\mathbf{u}=0, \tag{18}$$

$$c_t+\mathbf{u}\cdot\nabla c=0. \tag{19}$$

Here, $\mathbf{e}_g=(\cos\beta,-\sin\beta)$ and the function $\phi=\phi(c)$ interpolates linearly between -1 and $+1$ for $c\in[0,1]$. The two additional dimensionless parameters appearing above are the Reynolds number, Re, and the (densimetric) Froude number, Fr, defined as follows:

$$Re\equiv\frac{\hat{V}_0\hat{D}}{\hat{\nu}},\quad Fr\equiv\frac{\hat{V}_0}{\sqrt{At\hat{g}\hat{D}}}. \tag{20}$$

Here, $\hat{\nu}$ is defined using the mean density $\hat{\rho}=(\hat{\rho}_H+\hat{\rho}_L)/2$, and the mean static pressure gradient has been subtracted from the pressure before scaling. We see that for small At the flow is essentially governed by the three parameters β, Re, and Fr. For $t>0$, no slip boundary conditions are satisfied at the solid walls (zero flux for c) and outflow conditions imposed at the channel exit. At the inflow, the heavy fluid concentration is imposed ($c=0$), and the velocity $\mathbf{u}$ is represented by a fully established Poiseuille profile. The initial interface position is some way down the channel and our initial velocity field is stationary: $\mathbf{u}=0$ at $t=0$.

The model Eqs. (17)–(19) have been discretized using a mixed finite element/finite volume method. The Navier–Stokes equations are solved using the Galerkin finite element method, where the divergence-free condition is enforced by an augmented Lagrangian technique.[35] The computations are carried out on a structured rectangular mesh, with linear elements (Q1) for the velocity and constant elements (P0) for the pressure discretization. The concentration Eq. (19) uses a finite volume method. The advective terms are dealt with via a MUSCL scheme. On each timestep, a splitting method is used to advance the concentration equation over a number of

smaller subtimesteps. The present numerical algorithm is implemented in C++ as an application of PELICANS[36] (available at https://gforge.irsn.fr/gf/project/pelicans/).

Various simple test problems have been implemented. The code has also been benchmarked against that used by Sahu *et al.*,[32] which produces very similar results in our flow setup. After running each simulation, front velocities can be calculated from the spatiotemporal plot of c. Mesh refinement was carried out until successively calculated front velocities on meshes differed by 1%–4% (over the range of physical parameters explored). The meshes used for the computations presented below have 28 cells across the channel, refined slightly toward the walls, and 400 cells along the length of the channel. We acknowledge that the meshes used are relatively coarse, but note that the principle information being extracted from the simulations is bulk information, e.g., spatiotemporal plots and front speeds, which are less sensitive to refinement. There is numerical diffusion present in solution of Eqs. (17)–(19). Implementing molecular diffusion within Eq. (19) was also tested, i.e., by adding $(1/Pe)\nabla^2 c$ to the right-hand side. However, for the mesh sizes we have used it was found that for $Pe \geq 10^5$ there was no discernible difference in results; i.e., numerical diffusion is dominant. This range of Pe easily includes the experimental range.

Approximately 100 numerical simulations have been carried out in this low $\hat{V}_0$ range. We have selected a range of parameters that resembles that of our pipe flow experiments. Thus, we will describe the simulations in the following section with reference to $\hat{V}_0$, $\hat{V}_\nu$, and $\hat{V}_t$, as these are more natural from the experimental perspective. The mapping between parameters is simply

$$Re \equiv \frac{\hat{V}_0 \hat{V}_\nu}{\hat{V}_t^2}, \quad Fr \equiv \frac{\hat{V}_0}{\hat{V}_t}. \tag{21}$$

When considering the lubrication model predictions,

$$\chi = \frac{2\cos\beta \hat{V}_\nu}{\hat{V}_0} = \frac{2\,Re\cos\beta}{Fr^2}. \tag{22}$$

Unlike the pipe flow, we have limited our computational study to parameters for which the pure exchange flow ($\hat{V}_0 = 0$) is in the viscous regime. The reason for this restriction is that in general the stabilizing effect of the imposed flow[1] does not affect the channel exchange flow in the same way as it affects a pipe exchange flow. For the pure exchange flow, Hallez and Magnaudet[37] reported key differences in the flow structure for pipe and plane channel geometries when in the inertial regime.

C. Numerical results

Figure 10 gives an example of a displacement that is typical of those found close to the stationary interface regime, [parameters $\beta = 87°$, $\hat{\nu} = 2\times10^{-6}$ m$^2\cdot$s^{-1}, $At = 3.5\times10^{-3}$, and $\hat{V}_0 = 9.5$ mm$\cdot$s^{-1} ($Re = 90$, $Fr = 0.37$)]. The upper image in Fig. 10 depicts the initial condition for the concentration field at $\hat{t} = 0$ (s). The subsequent images (from top to down) show the evolution of the concentration field at $\hat{t} = 25$, 50, 100, 200, and 300 s. Although we observe that for $\hat{t} > 0$ the trailing front initially moves backward against the mean flow, for $t \geq 100$ the front appears stationary with the top of the interface seemingly pinned to the upper wall. We observe that downstream the height of the interface is $h \approx 0.7$, which is in good agreement with the analytical prediction from the lubrication model. Note that although numerical diffusion is well limited by the MUSCL scheme, dispersion due to (physical) secondary flows is not restricted. This accounts for the gray regions in Fig. 10.

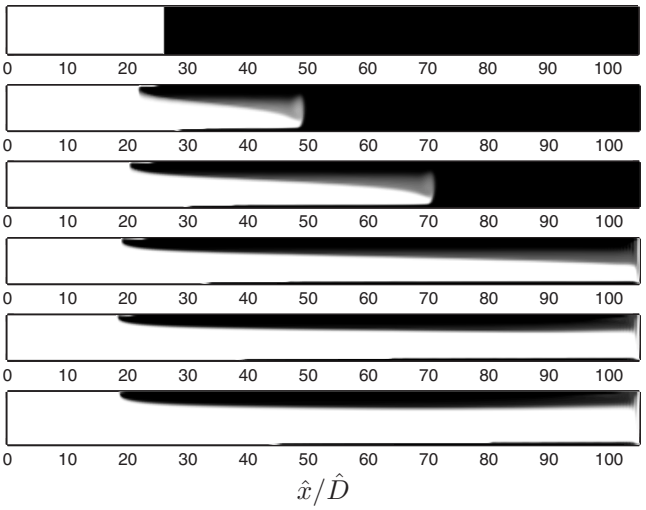

FIG. 10. Sequence of concentration field evolution obtained for $\beta = 87°$, $\hat{\nu} = 2\times10^{-6}$ m$^2\cdot$s^{-1}, $At = 3.5\times10^{-3}$, and $\hat{V}_0 = 9.5$ mm$\cdot$s^{-1} [$Re = 90$, $Fr = 0.37$]. The images are shown for $\hat{t} = 0$, 25, 50, 100, 200, and 300 s (from top to bottom).

To have a better understanding of the different regimes in typical stationary flows in a channel, Fig. 11 displays the spatiotemporal diagram of the average concentration along the channel for the same parameters as used in Fig. 10. In this diagram, the contrast has been slightly increased for illustrative purposes. We observe three characteristic behaviors. The slope of dashed line (1) represents the velocity of the leading front traveling toward downstream. The velocity of the trailing front (traveling upstream) is not constant with time. Initially, the trailing front flows backward with constant velocity shown by the slope of dashed line (2). As the front elongates, the velocity starts to decrease. We infer that inertial effects control the initial back flow velocity. The corresponding initial viscous velocity, which is proportional to the slope of the interface, would be too large (infinite at $\hat{t} \sim 0$). During the first acceleration when the interface between the two motionless fluids starts to move, the back flow is accelerated by buoyancy up until it attains approximately the inertial velocity. At this point inertia prevents the fluid from accelerating faster. When the trailing front stretches beyond a characteristic length, the viscous velocity becomes lower than the inertial velocity. At this point the back flow can dissipate its energy in the bulk by viscosity. Thereafter the back flow velocity starts to decrease and after a transient phase [between the lines (2) and (3) in Fig. 11], it reaches its limiting/final velocity. The dashed line (3) is almost vertical,

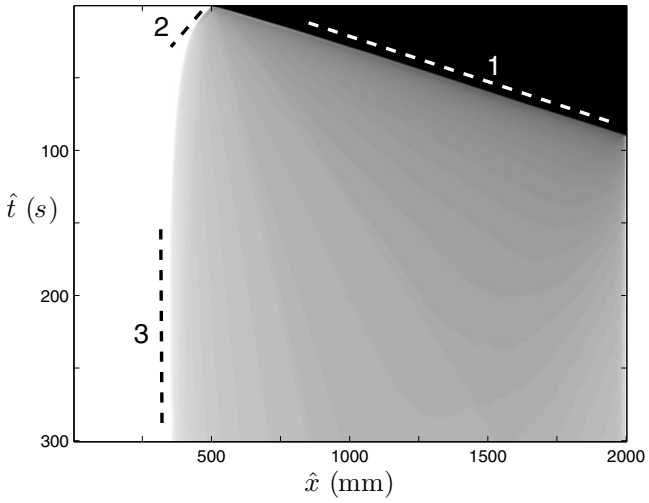

FIG. 11. Spatiotemporal diagram of the average concentration variations (white and black colors represent heavy and lighter fluids, respectively) along the channel for $\beta=87°$, $\hat{\nu}=2\times10^{-6}$ m$^2\cdot$s^{-1}, $At=3.5\times10^{-3}$, and $\hat{V}_0=9.5$ mm$\cdot$s^{-1} [$Re=90$, $Fr=0.37$]. Vertical scale: time; horizontal scale: distance along the channel. Dashed lines have slopes equal to velocities estimated for the front and back flows. The stationary slope (1) shows that the front velocity is constant. Dashed line (2) is the initial inertial velocity for the back flow, which is followed by a decreasing viscous velocity. Dashed line (3) is vertical, which implies that the lighter fluid velocity is zero (near-stationary).

which implies that the back flow velocity remains close to zero. The flow is in the stationary regime. Note that this is essentially the same picture that we have observed experimentally.

Figure 12 shows the velocity profiles corresponding to Fig. 10 at $\hat{t}=0$, 25, 50, 100, 200, and 300 s. The figure shows the region between $20<\hat{x}/\hat{D}<38$. The initial interface is located at $\hat{x}/\hat{D}=25$. As expected, for $\hat{t}<100$ we see a countercurrent flow in the longitudinal direction, with net flow equal to the imposed flow rate. In this time frame we transition from an initially inertially limited flow to a viscously limited flow.

Figure 13 illustrates a single velocity profile at $\hat{t}=300$ s at an axial position close to the pinned point, where the interface meets the upper wall. The local interface height ($h\approx0.775$) is shown by the dashed line, which is higher than the interface height downstream ($h\approx0.7$). We can observe the countercurrent flow inside the stationary upper layer.

Figure 14 displays the four archetypical regimes for different imposed flows. In Fig. 14(a), we see that for low imposed flow the velocity of the downstream front is constant at all times. The upstream front initially has a constant (inertially limited) velocity, which gradually decreases and finally reaches a constant buoyant velocity, allowing the

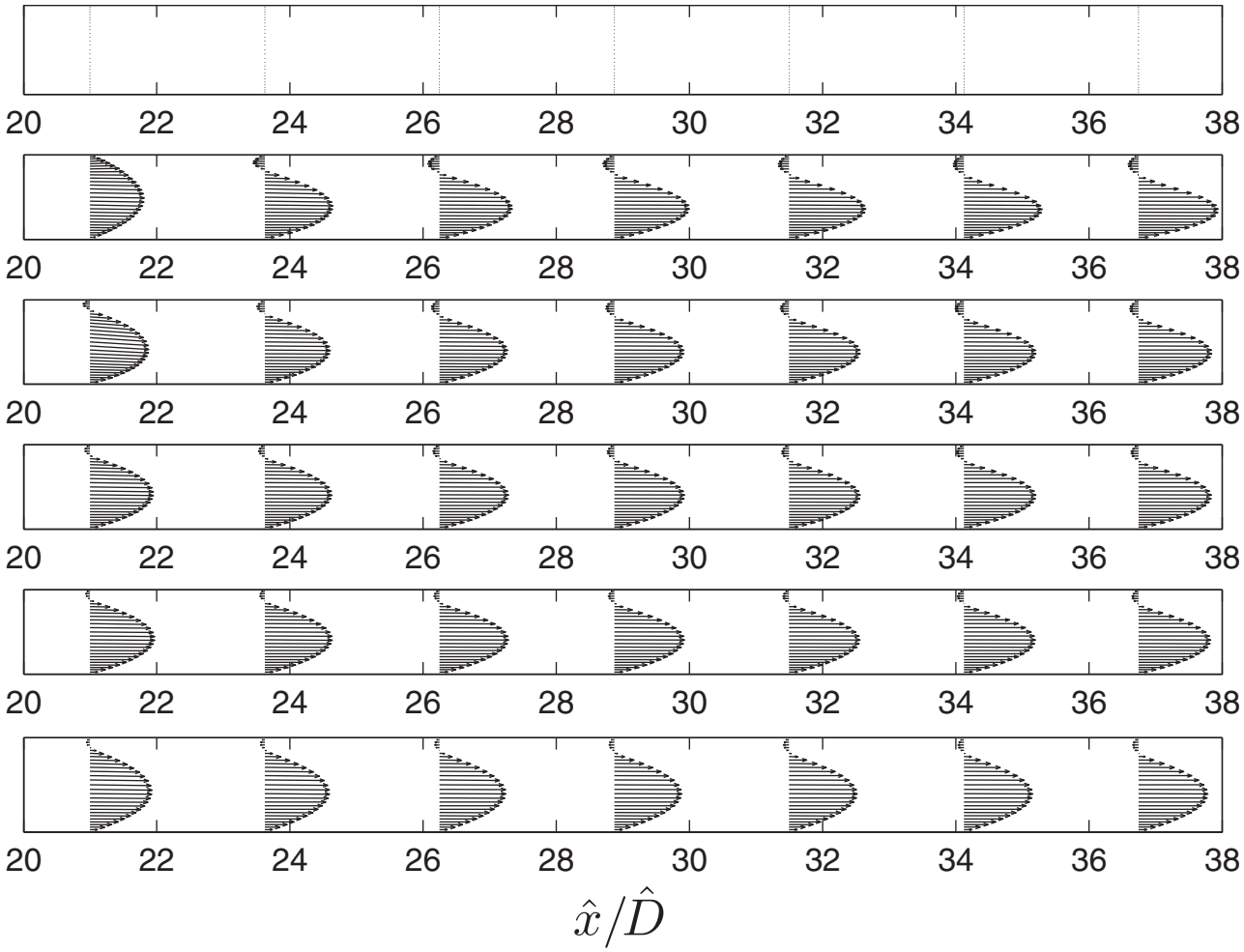

FIG. 12. The velocity profiles corresponding to Fig. 10 for a channel flow at $\hat{t}=0$, 25, 50, 100, 200, and 300 s (from top to bottom).

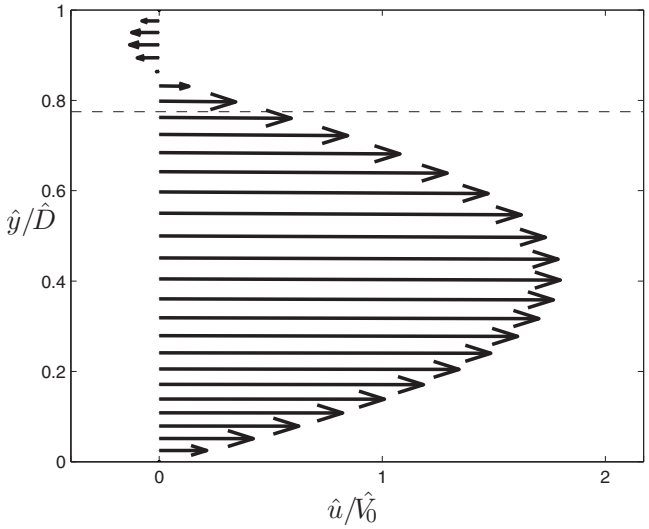

FIG. 13. The velocity profile close to the pinned point (with the axial position $\hat{x}/\hat{D}=26.25$) corresponding to Figs. 10 and 12 for a channel flow at $\hat{t}=300$ s: illustrating the countercurrent inside the stationary (lighter/black) fluid. Dashed line represents the local height of the interface.

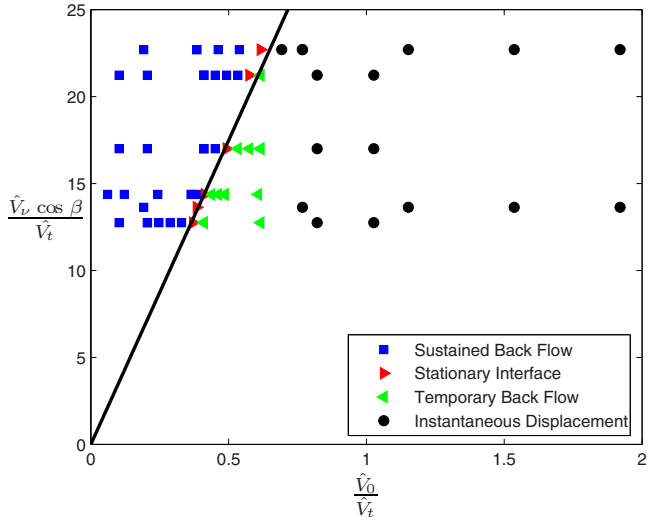

FIG. 15. (Color online) Classification of our simulation results in a channel. The heavy line represents the prediction of the lubrication model for the stationary interface: $34.97\,\hat{V}_0=\hat{V}_\nu\cos\beta$.

lighter fluid to keep rising (sustained back flow). Figure 14(b), at larger imposed flow velocity, is the stationary interface regime we have already examined in detail. A further increase in the imposed flow [Fig. 14(c)] leads to an upstream front, which advances, stops, and then recedes down the pipe. This corresponds to the temporary back flow regime. Finally, for a strong enough imposed flow [Fig. 14(d)], there is no back flow from the beginning of the displacement process. An instantaneous displacement is achieved.

Figure 15 shows the collected results of our simulations: $\hat{V}_0$ is in the range of $2-30$ mm·s^{-1}, At is in the range of $10^{-3}-10^{-2}$, $\hat{\nu}$ is in the range of $10^{-6}-2\times10^{-6}$ m^2·s^{-1}, and β is in the range of 85°–89°. Each simulation has been classified from the spatiotemporal plot as exhibiting one of the four characteristic behaviors. The bold line in Fig. 15 illustrates the analytical prediction of the stationary interface, for which $\hat{V}_\nu\cos\beta\approx34.97\hat{V}_0$ (i.e., $\chi=\chi_c=69.94$). We observe that there is good agreement between the lubrication model prediction and the stationary interfaces obtained by numerical simulation. This suggests that the two-layer model considered in the lubrication approximation is useful for predicting the long time behavior of buoyant channel displacements. In addition, the simulations representing the temporary back flows are clearly separated from those representing the instantaneous displacement flows. The transition between temporary back flows and the instantaneous displacement flows seems to be governed by a balance between the imposed pressure gradient (roughly speaking, $\hat{V}_0$) and the characteristic inertial velocity ($\hat{V}_t$). For viscous flow in a channel, this transition ($\hat{V}_0/\hat{V}_t=\gamma$) lies somewhere in the range of $\gamma=0.6-0.8$, probably with minor dependency on the inclination angle β.

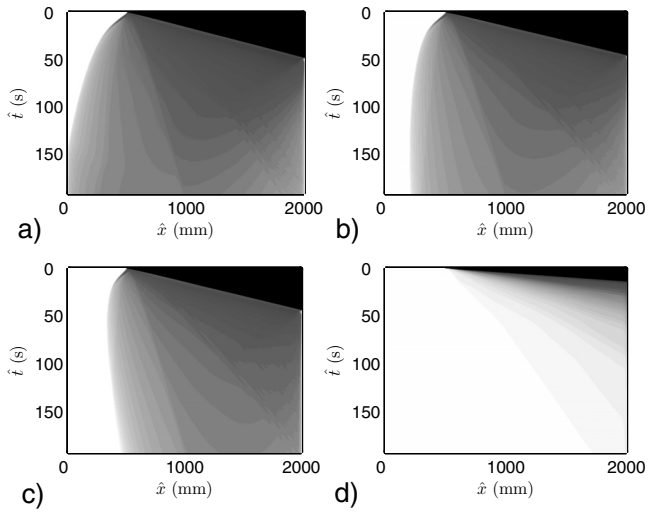

FIG. 14. Four possible conditions for a viscous buoyant channel flow in the presence of an imposed flow for $\beta=89°$, $\hat{\nu}=10^{-6}$ m^2·s^{-1}, and $At=10^{-2}$: (a) $\hat{V}_0=16.8$ mm·s^{-1} [$Re=323$, $Fr=0.39$]; (b) 18.9 mm·s^{-1} [$Re=363$, $Fr=0.44$]; (c) 21.0 mm·s^{-1} [$Re=403$, $Fr=0.49$]; (d) 78.6 mm·s^{-1} [$Re=1509$, $Fr=1.82$].

For flows in a more inclined channel, where the flow becomes inertial, we anticipate that there could be an increase in the value of γ. Experimental observations for an exchange flow in a pipe reveal that this increase can be up to 40% with respect to the horizontal.[2] Although the precise value of γ is of interest, it should be noted that this does not affect the long time behavior of the flow/interface. Indeed, whether or not the back flow is temporary or the displacement is instantaneous, the displacing fluid eventually washes out the displaced fluid as long as $\hat{V}_0/\hat{V}_\nu\cos\beta$ is large enough.

IV. CONCLUSIONS

We have observed an interesting displacement phenomenon in which a buoyant displacement flow retains a stationary upper layer of displaced fluid for the duration of our experiment. Unlike other stationary layers that have been

observed,[5,6,8] the fluid is fully mobile in the stationary layer. The net flux in the stationary layer is zero and the velocity of the interface (i.e., wavespeed) is also zero.

Our study reveals that this phenomenon marks the transition between flow parameters that displace fully and those that do not. Observations of the upstream region above the gate valve allow us to categorize the displacements as one of four different states: sustained back flow, stationary interface, temporary back flow, and instantaneous displacement. The stationary residual layers observed downstream coincide with the stationary interface regime observed for the upstream/trailing front. The same four states observed experimentally in the pipe are observed computationally in 2D computational simulations of plane channel displacements.

Instantaneous displacements and sustained back flow regimes can also be found at long times in thin-film/lubrication style models of these flows. The transition between states is the stationary layer, which is predicted by the lubrication model, at critical conditions

$$58.16\hat{V}_0 = \hat{V}_\nu \cos\beta \tag{23}$$

for the pipe geometry and

$$34.97\hat{V}_0 = \hat{V}_\nu \cos\beta \tag{24}$$

for a plane channel geometry. In the context of our previous study[1] where we have studied flow rate effects on the downstream front velocity, the stationary layer flows studied mark the boundary between the exchange flow dominated regime and the regime where the downstream front velocity ($\hat{V}_f$) increases linearly with $\hat{V}_0$, for which the imposed flow becomes increasingly dominant. The transition between temporary back flows and instantaneous displacements appears to be characterized by a condition $\hat{V}_0 = \gamma\hat{V}_t$, with $\gamma = 0.6-0.8$, for the plane channel geometry. This estimate has been made using only flow parameters for which the pure exchange flow would be viscous in the plane channel.

It is interesting to reflect that although we have classified four different states, in our experiments and in each of the models we have used we are only definitively able to identify three states. For the experimental results, we simply classify observed flows within the practical limits of our experiments. Thus, if the back flow exceeds the end of the pipe (above the gate valve), we classify it as a sustained back flow (although given a longer pipe some of these might be temporary), the stationary back flow is identified by there still remaining a stationary residual layer at the end of the experiment. The 2D plane channel computations are limited in much the same way as the experiments, in that computational times limit the range of feasible mesh sizes, computational domains, and time intervals to be investigated. The lubrication models have only been analyzed in the long time limit. In this limit the model exhibits in fact only three states: sustained back flow, stationary back flow, and instantaneous displacement. Although at short times (and distances) the model of Taghavi *et al.*[5] always has a fast initial phase where temporary back flows may exist, they are not present at long times. At short times the lubrication model assumptions are not immediately valid. This underlines the value of adopting a range of different techniques to understand the dynamics of complex flows: each technique gives different insights.

Among the four different states classified, the stationary interface is a transition state, only marking the flow that exists at the boundary between sustained and temporary back flow regimes. This means that it would be near impossible to find exactly the correct parameters to capture this state exactly. In all likelihood, any such state would finally evolve anyway into a temporary back flow via downstream processes such as fluid entrainment, thinning the layer below the critical thickness.

Thus, it is relevant that in our study we have observed (and classified as stationary) states that are probably only *close* to the transition state, but nevertheless persist for the duration of our experiments (physical or numerical). It is the existence of these near-stationary states, persisting over timescales of many thousand $\hat{D}/\hat{V}_0$, that have practical importance. Certainly such longevity could prove problematic for processes such as the primary cementing of near-horizontal oil and gas wells.

ACKNOWLEDGMENTS

This research has been carried out at the University of British Columbia, supported financially by NSERC and Schlumberger through CRD Project No. 354717-07. T. Séon also acknowledges additional financial support from PIMS through a postdoctoral fellowship. The authors thank S. Gharib for assisting in running the experiment. We thank A. Wachs and D. Vola for their assistance in introducing PELICANS. Finally, we thank the reviewers for their helpful comments and for alerting us to Ref. 6.

APPENDIX A: SIMPLE PHYSICAL MODEL

We close by showing that many qualitative features of our experiments can be predicted by a simplified conceptual model, along the lines of that presented by Séon *et al.*[2] for pure exchange flows. The objective is to describe the speed of propagation of the trailing front ($\hat{V}_f^{bf}$) and its position ($\hat{X}_f^{bf}$) as they move backward against the imposed flow.

First of all, it is clear that the only driving mechanism to push the lighter fluid up the channel is buoyancy. Except at early times, the flows above the gate valve appear quasiparallel [e.g., Figs. 3(b) and 3(c)], which suggests that the driving buoyancy force is balanced by viscosity. An appropriate velocity scale that reflects this balance is $\hat{V}_\nu$. Buoyancy acts both axially along the pipe ($\propto \cos\beta$) and perpendicular to the pipe axis ($\propto \sin\beta$). The latter transverse component acts only when the *interface* between the fluids is tilted with respect to the pipe axis (i.e., if $\partial\hat{h}/\partial\hat{x} \neq 0$) and is then proportional to $-\sin\beta\,\partial\hat{h}/\partial\hat{x}$. The second force affecting the back flow comes from the imposed flow, which determines a net pressure gradient pushing fluids downwards, along the pipe. Since the fluids are Newtonian we may assume that this force scales approximately linearly with $\hat{V}_0$. Therefore, on summing the different driving forces we might postulate that

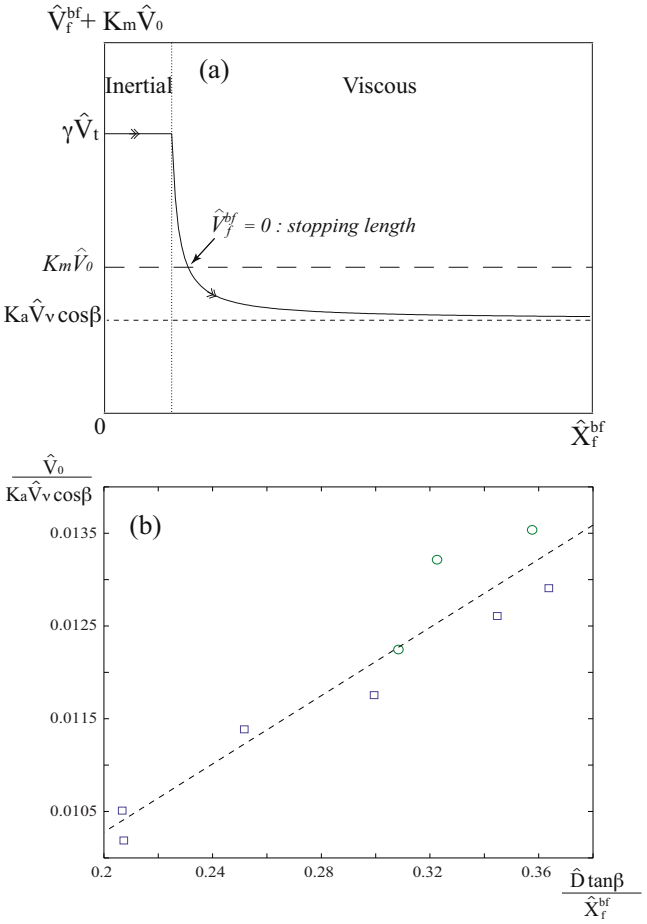

FIG. 16. (Color online) (a) Schematic variation of the velocity $\hat{V}_f^{bf}+K_m\hat{V}_0$ as a function of distance $\hat{X}_f^{bf}$ from the gate valve (continuous line) in a viscous regime and for $\beta\neq 90°$. The short dashed line represents the final viscous velocity $\hat{V}_f^{bf}+K_m\hat{V}_0=K_a\hat{V}_\nu\cos\beta$. The dotted line marks the boundary between the transient inertial regime and the viscous regime. We also represent the case $\gamma\hat{V}_t>K_m\hat{V}_0>K_a\hat{V}_\nu\cos\beta$, using the long dashed line, to underline the stopping length condition. The arrows on the curve show the trend of the evolution of the velocity with time. (b) $\hat{V}_0/(\hat{V}_\nu\cos\beta)$ is plotted vs $(\hat{D}/\hat{X}_f^{bf})\tan\beta$ for two series of experiments at different angles β: 83° (□) and 85° (○), and same density contrast and viscosity ($At=10^{-2}$, $\hat{\mu}=10^{-3}$ Pa·s). The experiments plotted here are either in the temporary back flow regime or in the stationary interface regime, and $\hat{X}_f^{bf}$ represents the position where the front stops (maximal $\hat{X}_f^{bf}$). The dashed line is a guide for the eye to show the common linear curve.

$$\hat{V}_f^{bf}=\hat{V}_\nu\cos\beta\left(K_a-K_t\frac{\partial\hat{h}}{\partial\hat{x}}\tan\beta\right)-K_m\hat{V}_0, \tag{A1}$$

where the coefficients K_a, K_t, and K_m reflect the relative influences of axial buoyancy, transverse buoyancy, and the mean flow, respectively. For the case $\hat{V}_0=0$ (exchange flow), this is the model of Séon *et al.*,[2] who estimated K_a and K_t from their experiments.

We see that the second term in Eq. (A1) decreases in size as the trailing front propagates, reducing the slope of the interface. Therefore, $\hat{V}_f^{bf}$ decreases with distance (and time) as is shown schematically in the *viscous regime* indicated in Fig. 16(a). Equation (A1) can be turned into a crude differential equation for $\hat{X}_f^{bf}$ by approximating the interface slope with $\partial\hat{h}/\partial\hat{x}\approx-\hat{D}/\hat{X}_f^{bf}$, which leads to

$$\frac{d\hat{X}_f^{bf}}{d\hat{t}}=\hat{V}_f^{bf}=\hat{V}_\nu\cos\beta\left(K_a+K_t\frac{\hat{D}}{\hat{X}_f^{bf}}\tan\beta\right)-K_m\hat{V}_0. \tag{A2}$$

At short times (and distances) the model Eq. (A2) would predict an infinite front velocity, which is not physically possible. In practice, in this early period of the flow $\hat{V}_f^{bf}$ will be limited by inertial effects rather than viscous effects. We may expect this balance to persist until the *viscous* front velocity, determined from Eq. (A2), falls below a value that is related to the inertial velocity scale, $\hat{V}_t$. We see for example that in Fig. 4 the front velocity is indeed initially constant before it decreases. This cut-off behavior is illustrated schematically in Fig. 16(a). Consequently, we may modify Eq. (A2) as follows:

$$\frac{d\hat{X}_f^{bf}}{d\hat{t}}=\min\left\{\gamma\hat{V}_t,\hat{V}_\nu\cos\beta\left(K_a+K_t\frac{\hat{D}}{\hat{X}_f^{bf}}\tan\beta\right)\right\}-K_m\hat{V}_0, \tag{A3}$$

where γ is a further coefficient to be determined.

Although simplistic, we believe that Eq. (A3) contains the essential elements of the trailing front dynamics. Evidently $\hat{V}_f^{bf}$ decreases with time as the front propagates, in all cases. Let us consider some different possible behaviors. First, let us suppose that the imposed flow is weak, so that $K_m\hat{V}_0<K_a\hat{V}_\nu\cos\beta$. The flow has a transient phase during which the interface slope decreases and the speed also, but the buoyancy force is strong enough to maintain a sustained back flow: $\hat{V}_f^{bf}\to K_a\hat{V}_\nu\cos\beta-K_m\hat{V}_0$ and the front advances steadily up the pipe. Second, suppose that the imposed flow is stronger, so that $K_m\hat{V}_0>K_a\hat{V}_\nu\cos\beta$, but that $K_m\hat{V}_0<\gamma\hat{V}_t$ [case represented in Fig. 16(a)]. The transient phase of the back flow elongates the interface so that the slope decreases until there is a perfect balance

$$\hat{V}_\nu\cos\beta\left(K_a+K_t\frac{\hat{D}}{\hat{X}_f^{bf}}\tan\beta\right)=K_m\hat{V}_0, \tag{A4}$$

corresponding to the stationary regime. Rearranging this shows that the stopping lengths X_f satisfy

$$\frac{\hat{V}_0}{\hat{V}_\nu\cos\beta}=\frac{1}{K_m}\left(K_a+K_t\frac{\hat{D}}{\hat{X}_f^{bf}}\tan\beta\right). \tag{A5}$$

Note that at larger $\hat{V}_0$ the transient phase of the back flow will be reduced, as will the stopping length. We might also expect that this delicate balance will be affected over longer times by changes in the interface profile below the gate valve, allowing the trailing front to recede down the pipe (which is not taken into account in our model). This is the temporary back flow regime. In this simple conceptual model, the stationary interface regime and the temporary back flow regime are both characterized by a stopping length, determined from Eq. (A5), which is the maximum height attained. The fully stationary layer is simply a mar-

ginal state that is theoretically present, but not easily observable. Finally, for still larger $\hat{V}_0$, say $K_m\hat{V}_0 > \gamma\hat{V}_t$, we expect no back flow and the instantaneous displacement regime is entered.

In Fig. 16(b), we have plotted $\hat{V}_0/(V_\nu \cos\beta)$ against $(\hat{D}/\hat{X}_f^{bf})\tan\beta$ for two series of experiments at different angles. Only those experiments are plotted that were characterized as a temporary back flow or stationary interface and $\hat{X}_f^{bf}$ is taken as the maximal measured front distance above the gate valve. We observe that the two series collapse approximately onto the same linear curve, as predicted by Eq. (A5). This supports the assumptions made regarding the driving forces of the buoyant back flow in the presence of a mean flow. In principle, this also allows us to determine directly the β-independent coefficients K_a/K_m and K_t/K_m, via linear regression, and to use the model in Eq. (A5) predictively. However, to be more confident in determining K_a/K_m and K_t/K_m we would need to conduct more experiments for a wider range of At, $\hat{\nu}$, and $\hat{D}$. The purpose of the model is instead to show that the types of behavior observed qualitatively can be attributed to a fairly simple force balance.

[1] S. M. Taghavi, T. Séon, D. M. Martinez, and I. A. Frigaard, "Influence of an imposed flow on the stability of a gravity current in a near horizontal duct," Phys. Fluids **22**, 031702 (2010).

[2] T. Séon, J. Znaien, J. P. Hulin, D. Salin, B. Perrin, and E. J. Hinch, "Transient buoyancy-driven front dynamics in nearly horizontal tubes," Phys. Fluids **19**, 123603 (2007).

[3] In this paper, we adopt the convention of denoting dimensional quantities with the ˆ symbol (e.g., the pipe diameter is $\hat{D}$) and dimensionless quantities without.

[4] T. Séon, J. P. Hulin, D. Salin, B. Perrin, and E. J. Hinch, "Buoyant driven miscible front dynamics in tilted tubes," Phys. Fluids **17**, 031702 (2005).

[5] S. M. Taghavi, T. Séon, D. M. Martinez, and I. A. Frigaard, "Buoyant-dominated slumping displacement flows in horizontal channels: The viscous limit," J. Fluid Mech. **639**, 1 (2009).

[6] H. E. Huppert and A. W. Woods, "Gravity driven flows in porous layers," J. Fluid Mech. **292**, 55 (1995).

[7] M. Carrasco-Teja, I. A. Frigaard, B. R. Seymour, and S. Storey, "Visco-plastic fluid displacements in horizontal narrow eccentric annuli: Stratification and traveling wave solutions," J. Fluid Mech. **605**, 293 (2008).

[8] M. Allouche, I. A. Frigaard, and G. Sona, "Static wall layers in the displacement of two visco-plastic fluids in a plane channel," J. Fluid Mech. **424**, 243 (2000).

[9] T. B. Benjamin, "Gravity currents and related phenomena," J. Fluid Mech. **31**, 209 (1968).

[10] J. E. Simpson, *Gravity Currents in the Environment and the Laboratory*, 2nd ed. (Cambridge University Press, Cambridge, UK, 1997).

[11] J. O. Shin, S. B. Dalziel, and P. F. Linden, "Gravity currents produced by lock exchange," J. Fluid Mech. **521**, 1 (2004).

[12] V. K. Birman, J. E. Martin, and E. Meiburg, "The non-Boussinesq lock-exchange problem. Part 2. High-resolution simulations," J. Fluid Mech. **537**, 125 (2005).

[13] V. K. Birman, B. A. Battandier, E. Meiburg, and P. F. Linden, "Lock-exchange flows in slopping channels," J. Fluid Mech. **577**, 53 (2007).

[14] D. Hoult, "Oil spreading in the sea," Annu. Rev. Fluid Mech. **4**, 341 (1972).

[15] N. Didden and T. Maxworthy, "The viscous spreading of plane and axisymmetric gravity currents," J. Fluid Mech. **121**, 27 (1982).

[16] E. E. Zukoski, "A review of flows driven by natural convection in adiabatic shafts," NIST Report No. NIST-GCR-95–679, 1995 and references therein; J. B. Cannon and E. E. Zukoski, "Turbulent mixing in vertical shafts under conditions applicable to fires in high rise buildings," Technical Fire Report No. 1, National Science Foundation, California Institute of Technology, Pasadena, California, 1975.

[17] M. H. I. Baird, K. Aravamudan, N. V. Rama Rao, J. Chadam, and A. P. Peirce, "Unsteady axial mixing by natural convection in vertical column," AIChE J. **38**, 1825 (1992).

[18] M. Debacq, V. Fanguet, J. P. Hulin, D. Salin, and B. Perrin, "Self-similar concentration profiles in buoyant mixing of miscible fluids in a vertical tube," Phys. Fluids **13**, 3097 (2001).

[19] M. Debacq, V. Fanguet, J. P. Hulin, D. Salin, B. Perrin, and E. J. Hinch, "Buoyant mixing of miscible fluids of varying viscosities in a vertical tube," Phys. Fluids **15**, 3846 (2003).

[20] T. Séon, J. P. Hulin, D. Salin, B. Perrin, and E. J. Hinch, "Buoyant mixing of miscible fluids in tilted tubes," Phys. Fluids **16**, L103 (2004).

[21] T. Séon, J. P. Hulin, D. Salin, B. Perrin, and E. J. Hinch, "Laser-induced fluorescence measurements of buoyancy driven mixing in tilted tubes," Phys. Fluids **18**, 041701 (2006).

[22] T. Séon, J. Znaien, J. P. Hulin, D. Salin, B. Perrin, and E. J. Hinch, "Front dynamics and macroscopic diffusion in buoyant mixing in a tilted tube," Phys. Fluids **19**, 125105 (2007).

[23] G. I. Taylor, "Dispersion of soluble matter in a solvent flowing slowly through a tube," Proc. R. Soc. London, Ser. A **219**, 186 (1953).

[24] R. Aris, "On the dispersion of a solute in a fluid flowing through a tube," Proc. R. Soc. London, Ser. A **235**, 67 (1956).

[25] P. Petitjeans and T. Maxworthy, "Miscible displacements in capillary tubes. Part 1. Experiments," J. Fluid Mech. **326**, 37 (1996).

[26] C.-Y. Chen and E. Meiburg, "Miscible displacements in capillary tubes. Part 2. Numerical simulations," J. Fluid Mech. **326**, 57 (1996).

[27] N. Rakotomalala, D. Salin, and P. Watzky, "Miscible displacement between two parallel plates: BGK lattice gas simulations," J. Fluid Mech. **338**, 277 (1997).

[28] Z. Yang and Y. C. Yortsos, "Asymptotic solutions of miscible displacements in geometries of large aspect ratio," Phys. Fluids **9**, 286 (1997).

[29] D. D. Joseph and Y. Renardy, "Fundamentals of two-fluid dynamics. Part 2: Lubricated transport, drops and miscible liquids," Interdisciplinary Applied Mathematics Series **4**, 0387979107 (1993).

[30] E. Lajeunesse, J. Martin, N. Rakotomalala, and D. Salin, "3D instability of miscible displacement in a Hele-Shaw cell," Phys. Rev. Lett. **79**, 5254 (1997).

[31] E. Lajeunesse, J. Martin, N. Rakotomalala, D. Salin, and Y. C. Yortsos, "Miscible displacements in a Hele-Shaw cell at high rates," J. Fluid Mech. **398**, 299 (1999).

[32] K. C. Sahu, H. Ding, P. Valluri, and O. K. Matar, "Pressure-driven miscible two-fluid channel flow with density gradients," Phys. Fluids **21**, 043603 (2009).

[33] E. B. Nelson and D. Guillot, *Well Cementing*, 2nd ed. (Schlumberger, Sugar Land, 2006).

[34] I. Grants, C. Zhang, S. Eckert, and G. Gerbeth, "Experimental observation of swirl accumulation in a magnetically driven flow," J. Fluid Mech. **616**, 135 (2008).

[35] R. Glowinski and P. Le Tallec, *Augmented Lagrangian and Operator-Splitting Methods in Nonlinear Mechanics* (SIAM, Philadelphia, 1989).

[36] PELICANS is an object oriented platform developed at IRSN, France, to provide general frameworks and software components for the implementation of partial differential equation solvers. PELICANS is distributed under the CeCILL license agreement.

[37] Y. Hallez and J. Magnaudet, "Effects of channel geometry on buoyancy-driven mixing," Phys. Fluids **20**, 053306 (2008).